

See discussions, stats, and author profiles for this publication at: <https://www.researchgate.net/publication/258806141>

Transition from Nanorod to Nanotube of Poly(vinylidene trifluoroethylene) Ferroelectric Nanofiber

ARTICLE *in* MACROMOLECULES · APRIL 2013

Impact Factor: 5.8 · DOI: 10.1021/ma302679g

CITATIONS

5

READS

49

5 AUTHORS, INCLUDING:



Yongri Liang

Beijing Institute of Petrochemical Technology

46 PUBLICATIONS 408 CITATIONS

SEE PROFILE



Kap Jin Kim

Kyung Hee University

90 PUBLICATIONS 1,286 CITATIONS

SEE PROFILE



Han Sup Lee

Inha University

33 PUBLICATIONS 534 CITATIONS

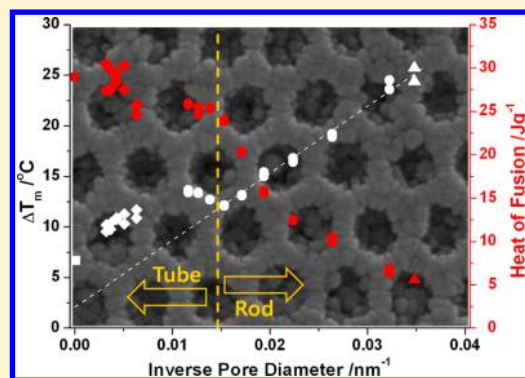
SEE PROFILE

Transition from Nanorod to Nanotube of Poly(vinylidene trifluoroethylene) Ferroelectric Nanofiber

Kiwoon Choi,[†] Se Cheol Lee,[†] Yongri Liang,[‡] Kap Jin Kim,[§] and Han Sup Lee^{*,†}[†]Department of Advanced Fiber Engineering, Inha University, Incheon 402-751, Korea[‡]Joint Laboratory of Polymer Science and Materials, The Beijing National Laboratory for Molecular Sciences, and Institute of Chemistry, Chinese Academy of Science, Beijing 100190, China[§]Department of Advanced Materials Engineering for Information & Electronics, Kyung Hee University, Yongin-si, Gyeonggi-do 446-701, Korea

S Supporting Information

ABSTRACT: The nanorod-to-nanotube transition of a piezoelectric poly(vinylidene fluoride-co-trifluoroethylene) (P(VDF-TrFE)) nanofiber inside cylindrical nanopores (CNP) with various pore diameters was precisely determined. After infiltrating the polymer into the CNP, a solid nanorod or hollow nanotube was obtained depending on the relative magnitude of the CNP diameter used compared to the critical pore diameter. The thickness of the lamellae formed inside the solid nanorod was found to be linearly dependent on the diameter of the nanocylinder. In addition, the wall thickness of the polymer nanotube increased with increasing nanocylinder diameter. The dependence of ferroelectric properties of the P(VDF-TrFE) nanofiber on the morphological transition were evaluated by measuring the piezoelectric polarization hysteresis loops. Compared to the hollow nanotube, the solid P(VDF-TrFE) nanorod showed significantly enhanced maximum polarization behavior, which is desirable for ferroelectric applications. These results show that the morphological transition from solid nanorod to hollow nanotube can play an important key role in the ferroelectric device fabrication of P(VDF-TrFE).



■ INTRODUCTION

Semicyralline polymers in one-dimensional (1D) nanostructures (nanofiber), such as nanorods and nanotubes showing nonclassical properties, can be promising candidates for advanced photonics, electronics, and mechanical and biomedical devices. The 1D nanostructures of ferroelectric polymers, such as poly(vinylidene fluoride) (PVDF) and its copolymer with trifluoroethylene (P(VDF-TrFE)), have attracted considerable attention for applications in sensors, energy storage, nanogenerators, and nonvolatile memory devices.^{1–4}

Many semicyralline polymers form lamellar crystals with thicknesses in the order of 10 nm, in which the folded polymer chains are preferentially aligned perpendicular to the lamellar fold surfaces. On a larger scale, the lamellae of polymers are generally organized to form a spherulite, which is a densely branched, isotropic polycrystalline superstructure.⁵ On the other hand, the formation of the spherulitic superstructure of polymers in a nanosized container might be suppressed due to geometric constraints (or nanoconfinement). Therefore, polymers with nanodimension have crystal qualities (crystal structure, crystal size, crystal orientation, and crystallinity) which can be significantly different from those in the bulk. The precise nature of the confining geometries of the nanofilm, nanorod, nanotube, and nanodot strongly affects the crystal

forming process of a polymer melt and plays a significant role in determining the crystal quality.^{3,6–20} Therefore, it is important to understand the geometry and size effects of nanoconfinement on the crystal structure of semicyralline/ferroelectric polymers to enhance/optimize the performance of functional devices in a range of applications.

A range of processing methods, such as template wetting, nanoimprint lithography, and microphase separation of block copolymers, have been developed for 1D nanostructure fabrication.^{21–23} Using the template wetting method, a 1D polymer nanostructure array with high order and density can be prepared easily by infiltrating a polymer melt or solution into inorganic nanopores in, for example, anodized aluminum oxide (AAO).^{21,22} AAO has been used extensively for studies of the confinement effect inside cylindrical nanopores because it can form very well-defined straight CNP with finely controlled pore dimensions.²⁴

During the crystallization of a polymer melt inside the CNP of AAO, it was reported that the growth of the lamellae along the radial direction of CNP could be suppressed by the nanoconfinement effect.^{6–14,17} Therefore, the crystal structures

Received: December 31, 2012

Revised: March 31, 2013

Published: April 10, 2013

formed inside the CNP could be quite different from those normally observed for the bulk.¹³ The crystal orientation was also affected by the curvature of the CNP. The crystals grew preferentially along the longitudinal direction, i.e., direction of minimum curvature of the cylindrical surface in AAO.^{6–14,17} The crystal quality depends strongly on the confinement size (pore dimension). As the pore diameter (D_p) of the CNP in AAO decreases, the degree of orientation increases with a concomitant decrease in crystal size and crystallinity.^{6,11,12} But it has also been reported that the opposite might occur when there is surface initiated crystallization.⁹ Studies on isotactic poly(propylene) confined within porous alumina membranes reported that the frustration driven by the nanoscopically constrained geometry induced nucleation-dominant crystallization.¹⁵ Homogeneous nucleation was dominant in the smaller size pores ($D_p < 65$ nm). On the other hand, the likelihood of heterogeneous nucleation increased for crystallization in the larger size pores. The precise size of the nanoconfinement system is one of the most important parameters determining the quality of the crystal formed inside the nanocontainers.

A polymer infiltrated into the CNP by surface wetting forms either a solid nanorod or hollow nanotube depending on the size of the pores in AAO.²⁵ This type of rod-to-tube transition with the confinement size can have a significant effect on the crystal quality as well as the optical, mechanical, and ferroelectric properties of the 1D nanostructures. Therefore, the rod-to-tube transition needs to be examined carefully for a precise understanding of the properties of 1D nanostructures.

EXPERIMENTAL SECTION

AAO Membrane Preparation. Three different groups of AAO templates were prepared by two-step anodization at applied voltages of 19 V (in 1 M H_2SO_4), 40 V (0.3 M $(COOH)_2$), and 195 V (0.1 M H_3PO_4), respectively, using aluminum disks (99.999%, Goodfellow) 15 mm in diameter and 0.5 mm in thickness. Seventeen AAO samples with D_p in the 16–320 nm range were prepared by a subsequent chemical etching process (30 °C, 0.3 M oxalic acid in deionized water). The process for fabricating AAO is described elsewhere.^{26,27}

Preparation of P(VDF–TrFE)-Filled AAO Membrane. The VDF/TrFE ratio in the P(VDF–TrFE) ($M_n = 79\,000$ g/mol, PDI = 1.37, Solvay) used was 70/30. A film, ~ 100 μ m in thickness, was prepared by melting P(VDF–TrFE) at 200 °C for 5 min and then applying a 2000 kgf force with a melt presser (Carver, 2697). To infiltrate P(VDF–TrFE) into the pores in the AAO template, all 17 AAO templates (depth: 50 μ m) were placed simultaneously on a hot plate in a vacuum chamber. After heating to 200 °C under vacuum ($<10^{-1}$ Torr), the polymer and AAO templates were maintained for 12 h for complete infiltration into the pores in AAO. After releasing the vacuum, the samples were quenched in water at room temperature. The remaining P(VDF–TrFE) film on the surface of the AAO was initially removed using a surgical blade. The residual P(VDF–TrFE) was dissolved chemically by dropping MEK solvent on the surface of the AAO template spinning at 8000 rpm on a spin-coater. The complete removal of P(VDF–TrFE) from the surface of the AAO template was confirmed by atomic force microscopy (AFM, Veeco, D3100). The aluminum base layer was then removed with a copper(II) chloride solution to finally obtain the P(VDF–TrFE)-filled AAO membrane samples.

Thermogravimetric Analysis (TGA). For TGA (TA, Q50), the AAO samples containing P(VDF–TrFE) polymer inside nanopores (about 13 mg) were heated from room temperature to 800 °C at 20 °C/min and maintained at 800 °C until the sample mass remains almost constant.

Differential Scanning Calorimetry (DSC). For DSC measurements (TA, Q200), the samples (about 13 mg) were heated to 200 °C,

held isothermally for 5 min, cooled to 0 °C at 10 °C/min, held isothermally for 5 min, and finally heated to 200 °C at 10 °C/min.

RESULTS AND DISCUSSION

From Solid Nanorod to Hollow Nanotube. In this study, the morphology of 1D nanostructures inside the CNP of AAO with various pore dimensions (D_p) was examined using P(VDF–TrFE) (Solvay, $M_n = 79\,000$ g/mol, PDI = 1.37, VDF/TrF = 70/30) as the model polymer. Three different groups of AAO templates with a 50/16, 105/31, and 501/158.4 nm interpore distance (D_{int})/initial D_p , and a 50 μ m depth were prepared by two-step anodization at applied voltages of 19, 40 and 195 V, respectively.²⁶ Seventeen AAO samples with D_p in the 16–320 nm range were prepared by a subsequent chemical etching process. (See Table 1 for the detailed dimensions of each sample.) The CNP dimensions (D_p , D_{int} , pore length) were evaluated by scanning electron microscopy (SEM).

Table 1. Electrolyte Type, Concentration, and Applied Voltage Used during the Anodization Process; Interpore Distances Obtained as a Result of the Anodization Process; Initial Pore Diameter and Porosity; Pore Diameters and Resulting Porosity Obtained after the Pore Widening Process (Interpore Distance (D_{int}), Pore Diameter (D_p), Porosity (P))

electrolyte	D_{int} (nm)	initial pore, D_p (P)	after pore widening, D_p (P)
H_2SO_4 19 V, 1.0 M	50	16 nm (9.3%)	22.4 nm (18.1%), 28.7 nm (29.9%)
$(COOH)_2$ 40 V, 0.3 M	105	31 nm (7.9%)	37.9 nm (11.7%), 44.7 nm (16.5%), 51.6 nm (21.9%), 58.5 nm (28.1%), 65.3 nm (35.1%), 72.2 nm (42.8%), 79.0 nm (51.4%), 85.9 nm (60.7%)
H_3PO_4 195 V, 0.1 M	501	158.4 nm (9.1%)	196.7 nm (14.0%), 235.0 nm (20.0%), 273.2 nm (27.0%), 311.5 nm (35.1%)

Figure 1 shows the nanostructures of P(VDF–TrFE), which were infiltrated by surface wetting into the CNP of the AAO template at 200 °C for 10 s, followed by quenching to room temperature. At the tips of the P(VDF–TrFE) nanostructures inside the CNP of 79, 158 nm D_p , small holes appear to be present, indicating the possible presence of hollow nanotubes. On the other hand, similar holes seem not to be observed for the P(VDF–TrFE) nanostructure inside the CNP of 31, 59 nm D_p , suggesting the possible formation of a solid nanorod. This type of morphological change could be understood based on the infiltration process mechanism of polymer materials.

As the polymer melt can wet the inner surface of the aluminum oxide CNP easily, either partial or complete wetting phenomenon occurs depending on the spreading coefficient (S), which is determined by the molecular weight of the polymer and process temperature used.²² S is defined as follows:

$$S = \gamma_{SG} - \gamma_{SL} - \gamma_{LG} \quad (1)$$

where γ_{SG} , γ_{SL} , and γ_{LG} represent the solid (CNP wall)–gas, solid–liquid (polymer melt), and liquid–gas interfacial tensions, respectively.²⁸ For $S < 0$ (normally observed at low temperature infiltration), partial wetting occurs and the polymer melt fills the pores through capillary action to form solid nanorods. For $S > 0$ (usually observed at high temperature infiltration), the precursor film of the polymer melt covers the

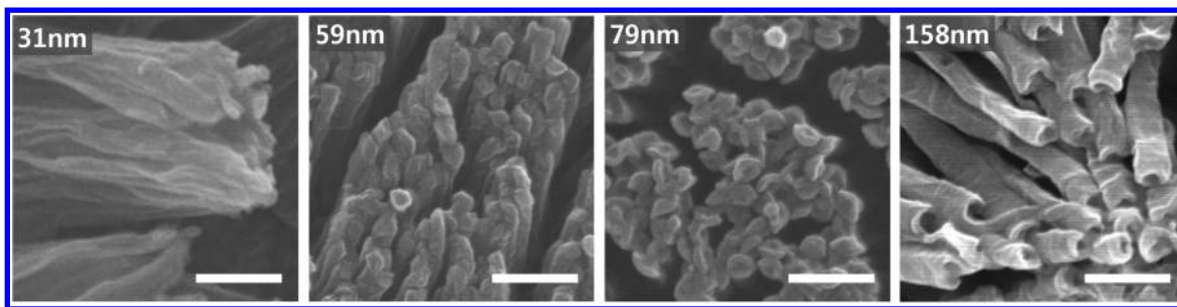


Figure 1. SEM images of four samples of different pore diameters showing the tip shape of the apparent solid nanorods (31 nm, 59 nm D_p) and hollow nanotubes (79 nm, 158 nm D_p). Scale bars are 300 nm.

inner walls of the CNP of AAO.²² A solid nanorod might be formed if the thickness of the precursor film is greater than the radius of the CNP ($D_p/2$).²⁵ Because the thickness of the precursor film is approximately 20–50 nm, a nanorod-to-nanotube transition is expected to occur at 40–100 nm D_p .^{10,21} For the infiltration of P(VDF–TrFE) at 200 °C, which is well above its melting temperature (T_m , 148 °C), complete wetting might occur. Therefore, a nanorod-to-nanotube transition might be observed at the critical D_p .

The SEM images in Figure 1 seem to indicate the presence of a nanorod-to-nanotube transition. Solid nanorods and hollow nanotubes might be obtained inside the CNP of $D_p \leq 59$ nm and $D_p \geq 79$ nm, respectively. But, SEM observation might not be sufficient for the precise determination of the nanorod-to-nanotube transition because small hole at the tip of the nanotube might be blocked by the metal film evaporated for SEM observations. An additional method is needed to confirm the nanorod-to-nanotube transition and for a precise evaluation of the critical D_p dimension separating solid nanorod from hollow nanotube formation.

Wetted polymer resides inside the CNP of an AAO membrane on the bottom aluminum, which can be dissolved away chemically. TGA of the P(VDF–TrFE) filled AAO membrane can be used to measure the mass of P(VDF–TrFE) separately. If hollow tubes are formed inside the CNP, the polymer mass would be smaller than the corresponding solid nanorod due to the empty region of the nanotube. Therefore, the nanorod-to-nanotube transition can be identified precisely by calculating the ratio of the polymer mass inside the CNP to the total mass (mass of P(VDF–TrFE) filled AAO membrane).

For TGA, P(VDF–TrFE) was infiltrated into CNP of AAO at 200 °C for 12 h, and the residual P(VDF–TrFE) at the surface of the AAO membrane was removed. Figure 2a shows an SEM image of the surface of the P(VDF–TrFE) filled AAO membrane sample. Complete removal of the polymer remaining at the surface of the membrane was also confirmed by AFM. The complete filling of P(VDF–TrFE) to the tip of the CNP was confirmed by SEM observations of the AAO membrane cross section.

Figure 2b shows the mass percentage (PM%) of the polymer samples inside the AAO membrane of 16–320 nm D_p as a function of the porosity (P) of CNP, which can be calculated using eq 2. Here, P is the CNP pore area/total surface area of the AAO membrane, which corresponds approximately to CNP pore volume (pore area \times depth)/total volume (total area \times depth).

$$P = \frac{2\pi}{\sqrt{3}} \left(\frac{r}{D_{\text{int}}} \right)^2 \quad (2)$$

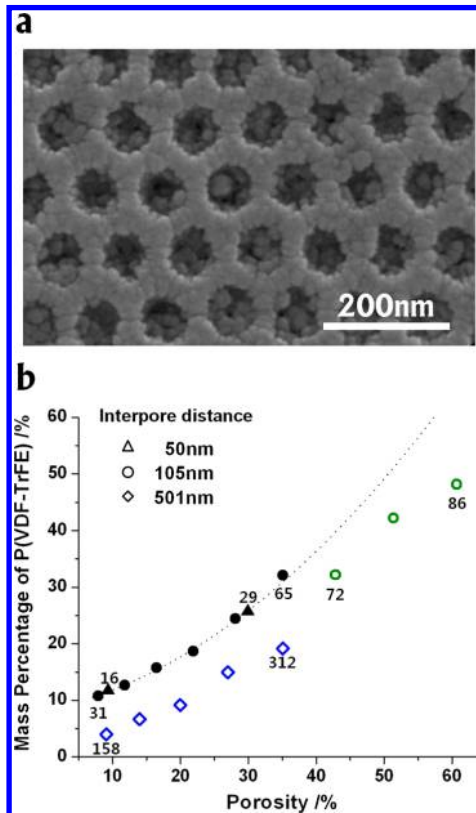


Figure 2. (a) SEM image showing the surface of P(VDF–TrFE) filled AAO. Complete removal of the remaining P(VDF–TrFE) from the surface was confirmed. (b) Mass percentage of P(VDF–TrFE) in all samples used as a function of the porosity in AAO. Actual pore diameters (D_p in nm) of some selected samples are noted in the figure. Black, green, and blue data points correspond to group I, II, and III, respectively.

PM% is the P(VDF–TrFE) mass/total mass (P(VDF–TrFE)-filled AAO membrane) obtained from the mass at 800 °C during the TGA experiment. Approximately 0.28% of the initial P(VDF–TrFE) and 99.99% of the initial AAO membrane mass remained at 800 °C. If a polymer is infiltrated into the CNP of AAOs with identical porosity, identical PM% will be obtained for all samples regardless of its D_{int} and pore length, only if all the samples form solid nanorods. If hollow nanotube is formed, the PM% will be smaller than the corresponding nanorod.

The three AAO samples had a D_{int} of 50, 105, and 501 nm, which had been anodized at 19, 40, and 195 V, respectively, and had a corresponding 16, 31, and 158 nm D_p . According to the “10% porosity rule”, all three samples before the pore widening process had ~10% porosity.²⁶ Although the PM% of the CNP

with both 16 and 31 nm D_p was $\sim 10\%$, the PM% of the CNP with 158 nm D_p was $\sim 4\%$, which is significantly smaller than the previous two samples. This suggests that there might be empty space in the polymer inside the CNP of 158 nm D_p . Therefore, solid nanorods were formed inside the CNP of 15 and 31 nm D_p , and hollow nanotubes were formed inside CNP of 158 nm. As shown in Figure 2b, the PM% of the data points (shown in black in group I) increase gradually with increasing porosity, as expected. On the other hand, all data points of the CNP with $D_p \geq 158$ nm (shown in blue in group III) remained well below the black data points (group I), indicating the formation of hollow nanotubes. With increasing D_p from 65 to 72 nm, the PM% remained almost constant and did not follow the gradual increase (shown with dotted line in Figure 2). All data points of 72–86 nm D_p (group II, shown with green data points) remained below the dotted line. These results suggest that the samples in group I (16–65 nm D_p) form solid nanorods, a nanorod-to-nanotube transition occurs between 65 and 72 nm, and the samples in groups II and III (72 nm and above D_p) form nanotubes. This is consistent with the SEM observations shown in Figure 1.

Frustrated Crystallization inside Nanofiber. For DSC, another set of samples were prepared using the method used for the previous TGA experiment. To remove any thermal history, all samples were heated to well above the T_m of P(VDF–TrFE), followed by cooling to room temperature at a cooling rate of 10 °C/min to allow the nonisothermal crystallization of the polymer inside the CNP. Figure 3a shows the DSC thermograms of P(VDF–TrFE) samples inside the pores of the AAO membrane obtained during the subsequent heating process (10 °C/min heating rate). All thermograms showed two endothermic peaks. The peaks at 70–110 °C correspond to the Curie transition (transition of ferroelectric phase to paraelectric phase), and the peaks above 110 °C correspond to the melting transition. The T_m of the crystal was obtained from the onset temperature of the peaks. The T_m of bulk P(VDF–TrFE) was 148.1 °C. As the size of the CNP (D_p) decreases from 312 to 16 nm, the T_m changed from 145.3 to 112.6 °C. The T_m depression in Figure 3a can be interpreted in terms of the decreased crystal size induced by the confinement effect of the CNP.

Assuming a rectangular-shaped lamellar crystal, the relationship between the T_m of the crystal and crystal dimensions can be described well by the Gibbs–Thomson equation (eq 3).⁵

$$\Delta T_m = T_m^\circ - T_m = \left(\frac{\gamma_e}{l} + \frac{\gamma_1}{x} + \frac{\gamma_2}{y} \right) \frac{2T_m^\circ}{\Delta H_v} \quad (3)$$

where T_m° is the T_m of an infinitely large crystal (equilibrium T_m), γ_e is the surface energy of the fold surfaces at the top and bottom of the lamellar crystal, γ_1 and γ_2 are the surface energies of two fold planes, and l , x , and y are the thickness, width, and length of lamella, respectively. ΔH_v is the heat of fusion of the lamella. In the case of bulk materials, x and y are significantly greater than l . Therefore, last two terms in eq 3 can be neglected and the T_m depression (ΔT_m) can be related to the reciprocal lamellar thickness.

A previous study reported (refer to Supporting Information) that the thickness direction of the P(VDF–TrFE) lamellae inside the CNP of AAO was along the radial direction of the CNP and lamellar crystal grows preferentially along the longitudinal direction of CNP.¹¹ The growth of a lamellar crystal along the radial direction of the CNP will be restricted

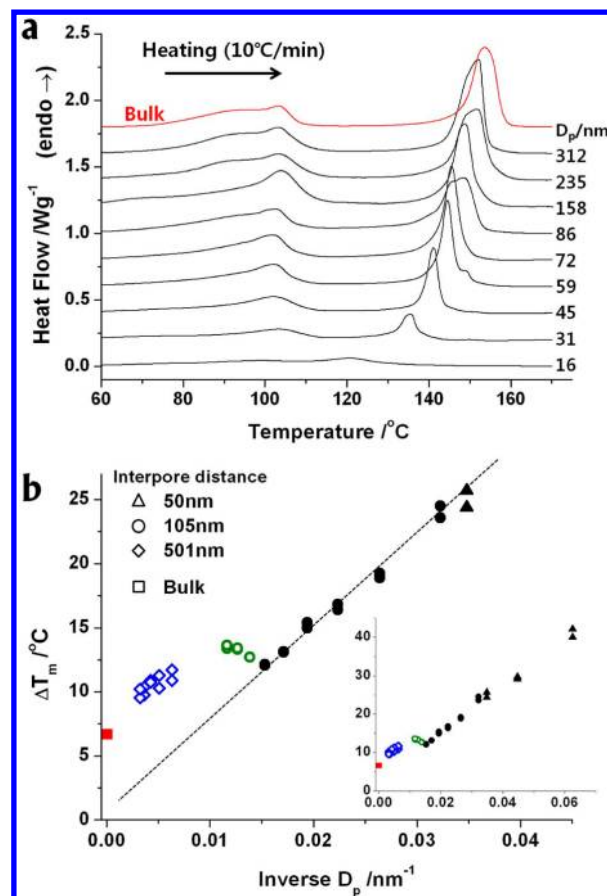


Figure 3. (a) DSC thermograms of the P(VDF–TrFE) samples inside the CNP of AAO. These were obtained during heating (10 °C/min) of the P(VDF–TrFE) samples, which had been crystallized by cooling from 190 °C to room temperature (–10 °C/min). (b) Melting temperature depressions ($\Delta T_m = T_m^\circ - T_m$) as a function of the inverse pore diameter ($1/D_p$) for some selected samples. A similar plot for all samples used is shown in the inset. Black, green, and blue data points correspond to group I, II, and III, respectively.

significantly by geometric constraints. Therefore, only one term out of the last two terms in eq 3 can be neglected for lamellar crystals formed inside the CNP of AAO.

$$\Delta T_m = T_m^\circ - T_m = \left(\frac{\gamma_e}{l} + \frac{\gamma_1}{x} \right) \frac{2T_m^\circ}{\Delta H_v} \quad (4)$$

According to classical primary nucleation theory, the critical sizes of a rectangular nucleus (l^* and x^*) can be expressed as follows:^{16,20}

$$l^* = \frac{4\gamma_e}{\Delta G_v} \quad \text{and} \quad x^* = \frac{4\gamma_1}{\Delta G_v} \quad (5)$$

where ΔG_v is the change in Gibbs free energy upon crystallization of the unit volume of a polymer melt. Because crystal growth along the radial direction of the CNP in AAO was suppressed by geometrical constraints resulting in nucleation-dominant crystallization,^{12,15,16} the actual crystal dimension (l , x) along the radial direction would be similar to the critical dimensions (l^* and x^*) defined in eq 5. Hence, $l \approx l^*$ and $x \approx x^*$ and $\gamma_e/l^* = \gamma_1/x^*$ based on eq 5. The two terms in eq 4 would be close to each other. Therefore, ΔT_m of the crystal in the CNP in AAO is proportional to the reciprocal thickness of the lamella.

$$\Delta T_m \propto \frac{1}{l} \quad (6)$$

Figure 3b shows the ΔT_m as a function of the inverse of the pore diameter ($1/D_p$) of CNP in AAO for all 17 samples studied. T_m° was calculated based on the T_m obtained from the DSC thermograms and Hoffman–Weeks equation (see the Supporting Information for details). The data points in group I (shown in black color) corresponding to the solid nanorods remain on the linear line that appears to be extrapolated to the origin. This suggests that $1/D_p \propto 1/l$. Therefore, the lamella thickness inside the CNP is proportional to the diameter of the CNP for the solid nanorods of 16–65 nm diameter ranges. Compared to the lamella thickness of the bulk, thinner lamellae were formed inside the CNP with smaller diameters.

A further increase in D_p from groups I to II (green data points in Figure 3b) resulted in a slight increase in ΔT_m . The deviation of the data in group II from linearity in Figure 3b can be understood in terms of the nanorod-to-nanotube transition, which is shown schematically in Figure 4. If a hollow nanotube

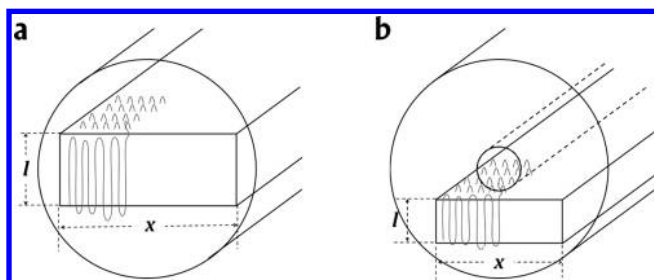


Figure 4. Schematic diagram showing the lamella of the maximum size inside a solid nanorod (a) and hollow nanotube (b) of an identical pore diameter.

is formed, additional empty space at the center of the CNP would serve as an additional geometrical constraint compared to the solid nanorod of an identical D_p . As shown schematically in Figure 4, the maximum lamella dimensions (l , x) permissible in the hollow nanotube would be smaller than the corresponding ones in the solid nanorod. Therefore, the slight increase in ΔT_m upon a nanorod-to-nanotube transition after a change from group I to group II appears to be consistent with the results in Figure 3b.

A further increase in D_p in group III (shown in blue data points in Figure 3b) decreased the ΔT_m gradually. The data in group III was extrapolated to ΔT_m of the bulk shown in the red square. If the wall thickness of the hollow nanotube is constant irrespective of D_p of the CNP in AAO, the dimensions (l , x) of the lamellae formed inside the hollow nanotube would not vary significantly with D_p of the CNP. The gradual decrease in ΔT_m for the data in group III suggests that the wall thickness of the hollow nanotube increases with D_p of the CNP. The wall thickness of the hollow nanotube could be estimated using the mass analysis data in Figure 2. (See the Supporting Information for details.) As the diameter of the CNP was increased from 158 to 312 nm, the wall thickness increased from approximately 14 to 49 nm, respectively. This mass analysis data on the wall thickness is consistent with the decreasing ΔT_m behavior of the data in group III (Figure 3b).

The degree of crystallinity (X_c) of the P(VDF–TrFE) inside CNP of AAO can be obtained from the melting transition peaks in Figure 3a and eq 7.

$$X_c = \frac{\Delta H_m}{\Delta H_{m,bulk}} X_{c,bulk} \quad (7)$$

where ΔH_m is the heat of fusion obtained from the DSC thermogram, $\Delta H_{m,bulk}$ is heat of fusion of bulk P(VDF–TrFE), and $X_{c,bulk}$ is X_c obtained from the wide-angle X-ray experiment. The X_c of the P(VDF–TrFE) inside the CNP of AAO can be obtained because the actual mass of P(VDF–TrFE) inside CNP can be obtained precisely from TGA. Figure 5 shows the

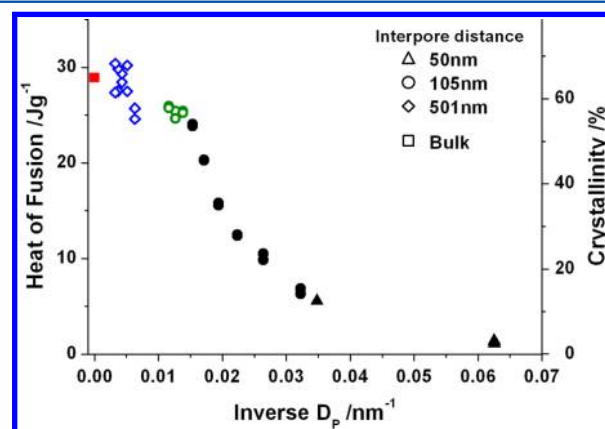


Figure 5. Heat of fusion (left ordinate) and crystallinity (right ordinate) of P(VDF–TrFE) samples in the CNP of AAO as a function of the inverse pore diameter. The inter-pore distances are displayed. Black, green, and blue data points correspond to group I, II, and III, respectively.

heat of fusion and crystallinity of all the samples used as a function of the inverse pore diameter ($1/D_p$). The X_c of P(VDF–TrFE) of 15 nm D_p was $\sim 2.0\%$. As the diameter was increased to 65 nm, X_c rapidly reached up to 80% of the bulk. A further increase in D_p to the data points in groups II and III resulted in significant reduction in the rate of increase. Although the data in group III are somewhat scattered, the X_c of the hollow nanotube of 320 nm D_p is close to the X_c of the bulk. The heat of fusion data also showed a distinctive difference between the solid nanorods and hollow nanotubes.

PVDF and P(VDF–TrFE) showed similar crystal phase behavior. Moreover, the polar β -crystal phase is the most highly polar phase that corresponds to all-trans (*tttt*) chain conformation desirable for many ferroelectric applications.^{1–4} Additional processes, such as mechanical stretching, high compression, hygroscopic salt, and microimprinting, are needed to obtain polar β - or γ -crystal phases because PVDF forms a nonpolar α -crystal phase with a tg^+tg^- chain conformation at room temperature.^{13,29–32} On the other hand, P(VDF–TrFE) crystallizes to the β -crystal phase spontaneously at room temperature due to the additional fluorine atom in TrFE, which sterically hinders the formation of tg^+tg^- formation in the α -crystal phase. The ferroelectric properties of P(VDF–TrFE) were retained under the extreme nanoconfinement, for example, in a film with a 1 nm thickness.³³ As reported by Lutkenhaus et al., a highly oriented β -crystal phase was obtained inside the cylindrical pores of AAO and crystal growth occurred preferentially along the direction of the minimum curvature direction of the cylindrical pores when hot-crystallized from the melt.¹¹ As shown in Figure S3, similar crystal orientations could be confirmed for all P(VDF–TrFE) samples inside the CNP of 31–86 nm D_p . The ferroelectric

property of P(VDF-TrFE) was affected significantly by the crystal quality, such as the crystal size, crystal orientation, and crystallinity.^{34–38} Therefore, the ferroelectric properties of P(VDF-TrFE) inside the CNP would also depend on the confinement size and geometry.

Effect of the Morphological Transition on the Ferroelectric Property. To determine the effect of a nanorod-to-nanotube transition on the ferroelectric performance of P(VDF-TrFE), a ferroelectric capacitor was prepared by depositing a top platinum electrode (100 nm thickness) on the P(VDF-TrFE) filled AAO membrane on an aluminum base layer using a $200 \times 200 \mu\text{m}$ shadow mask, which is shown schematically in Figure 6a. The polarization hysteresis loop in

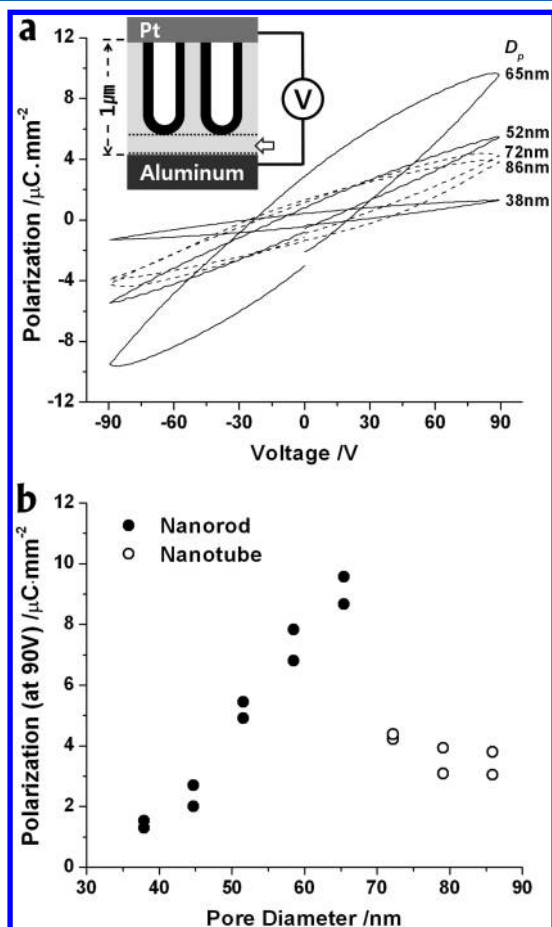


Figure 6. (a) Piezoelectric hysteresis loops measured with the ferroelectric capacitor of P(VDF-TrFE) filled AAO membrane having CNP of 38–86 nm D_p . Schematic diagram of the capacitor used is shown in the inset. (b) Polarization value obtained at 90 V applied voltage as a function of the CNP pore diameter.

the -90 to 90 V range was measured using a virtual ground circuit (Radiant Technologies Precision LC unit). Polarization value is Q/A , where Q is surface charge and A is actual cross-sectional pore area covered by the metal electrode. If D_{int} of the AAO templates used varies, the thickness of the alumina barrier layer between the bottom aluminum layer and P(VDF-TrFE) layer (denoted as the arrow in the schematic diagram in Figure 6a) changes significantly. Then, the effective voltage actually applied to the P(VDF-TrFE) layer might be affected by the D_{int} of the samples used, obscuring the measured polarization value. Therefore, only the P(VDF-TrFE) samples in the CNP

of 105 nm D_{int} with a $1 \mu\text{m}$ AAO thickness were used for the polarization measurements. Because the D_p of the samples used in this polarization experiment varied from 31 to 86 nm, it was expected that the effect of the nanorod-to-nanotube transition on the ferroelectric properties would be observed.

Figure 6a shows the piezoelectric hysteresis loops measured with the ferroelectric capacitor of an AAO membrane with a CNP of 31–86 nm D_p . Because of the high aspect ratio of the 1D nanostructures inside the AAO, the magnitude of the actual electric field applied to the P(VDF-TrFE) was relatively small compared to the usual thin film capacitor with a thickness less than 50 nm. The polarization hysteresis loop shown in Figure 6a suggests that the dipole has been poled along the direction of the electric field applied. A similar experiment carried out with the polystyrene filled AAO capacitor did not exhibit hysteresis loop behavior. The P(VDF-TrFE) capacitor inside CNP of 31 nm D_p had very low crystallinity and did not show any hysteresis loop. The saturation of the polarization value, which is normally observed in thin film P(VDF-TrFE) capacitors, was not observed because the actual magnitude of the electric field applied to P(VDF-TrFE) was low.

Figure 6b shows the polarization observed at a 90 V applied voltage along with the CNP diameter. To demonstrate the reproducibility, the polarization measurements were carried out twice with two different sets of samples and both data sets are shown in the Figure 6b. The polarization increased rapidly with increasing CNP diameter from 38 to 65 nm. With a further increase in CNP to 72 nm, the polarization value decreased abruptly and maintained a relatively low value for all samples with CNP diameters greater than 72 nm. As the polarization value can be affected directly by the crystal quality of P(VDF-TrFE) inside CNP, the results in Figure 6b can be interpreted in terms of the nanorod-to-nanotube transition occurring somewhere between 65 and 72 nm, as inferred from the thermal data shown in Figures 2 and 3. In the case of solid nanorods in the CNP of AAO, the crystal size and crystallinity increased rapidly with increasing D_p , resulting in an enhancement of the ferroelectric properties. If hollow nanotubes were formed, as in the CNP of 72–86 nm D_p , the ferroelectric performance is suppressed due to the reduced P(VDF-TrFE) mass and additional empty space at the center of the CNP. The reduced crystal quality, which can be confirmed from the lowered T_m in Figure 3b, upon transition from solid nanorod to hollow nanotube appears to impede the rotation of C–F dipoles in the β -crystal phase of P(VDF-TrFE) upon the application of an external electric field during the poling process. The precise morphology of the 1D nanostructure (either solid nanorod or hollow nanotube) might play an important role in determining the ferroelectric properties of P(VDF-TrFE). Therefore, a morphological study is needed to develop ferroelectric devices based on 1D nanostructures.

CONCLUSIONS

The transition from a solid nanorod to a hollow nanotube was precisely determined with P(VDF-TrFE) infiltrated into the CNP of AAO with diameters between 65 and 72 nm. The crystal quality inside the CNP was strongly affected by the nanorod-to-nanotube transition. In the case of the 15–65 nm D_p nanorod, the lamellar thickness was linearly dependent on the diameter of the CNP, and the crystallinity increased from 2.0% (15 nm D_p) to 80% of the bulk (65 nm D_p). For nanotubes inside the CNP of 72–312 nm D_p , the crystallinity was related to the wall thickness of the nanotube. The

morphological transition from a solid nanorod to a hollow nanotube played an important role in determining the ferroelectric properties of 1D nanostructures of P(VDF-TrFE). Overall, the molecular and morphological structures in 1D nanostructure need to be tailored finely to achieve the optimum performance of ferroelectric devices containing P(VDF-TrFE).

■ ASSOCIATED CONTENT

■ Supporting Information

Equilibrium melting temperature of P(VDF-TrFE) and analysis of wall thickness of hollow nanotube and the crystal orientation of P(VDF-TrFE) in the cylindrical nanopores. This material is available free of charge via the Internet at <http://pubs.acs.org>.

■ AUTHOR INFORMATION

Corresponding Author

*E-mail: hslee@inha.ac.kr.

Notes

The authors declare no competing financial interest.

■ ACKNOWLEDGMENTS

This work was supported by Basic Science Research Program through the National Research Foundation of Korea (NRF) grant funded by the Korea government (MEST) (616-2011-2-D00039). This work was supported by MEST and PAL, Korea. The experiments at PLS were supported in part by MEST and POSTECH. This work was also supported by an INHA Research Grant.

■ REFERENCES

- (1) Chang, C.; Tran, V. H.; Wang, J.; Fuh, Y.-K.; Lin, L. *Nano Lett.* **2010**, *10*, 726.
- (2) Cha, S. N.; Kim, S. M.; Kim, H. J.; Ku, J. Y.; Sohn, J. I.; Park, Y. J.; Song, B. G.; Jung, M. H.; Lee, E. K.; Choi, B. L.; Park, J. J.; Wang, Z. L.; Kim, J. M.; Kim, K. *Nano Lett.* **2011**, *11*, 5142.
- (3) Hu, Z.; Tian, M.; Nysten, B.; Jonas, A. M. *Nat. Mater.* **2009**, *8*, 62.
- (4) Mandal, D.; Yoon, S.; Kim, K. J. *Macromol. Rapid Commun.* **2011**, *32*, 831.
- (5) Strobl, G. *The Physics of Polymers*; Springer-Verlag: Berlin, 2007.
- (6) Park, K.; Choi, K.; Lee, J. H.; Park, S. H.; Lee, S. C.; Lee, H. S. *ACS Macro Lett.* **2012**, *1*, 110.
- (7) Ma, Y.; Hu, W.; Hobbs, J.; Reiter, G. *Soft Matter* **2008**, *4*, 540.
- (8) Wu, H.; Wang, W.; Huang, Y.; Su, Z. *Macromol. Rapid Commun.* **2009**, *30*, 194.
- (9) Li, M.; Wu, H.; Huang, Y.; Su, A. *Macromolecules* **2012**, *45*, 5196.
- (10) Steinhart, M.; Senz, S.; Wehrspohn, R. B.; Gösele, U.; Wendorff, J. H. *Macromolecules* **2003**, *36*, 3646.
- (11) Lutkenhaus, J. L.; McEnnis, K.; Serghei, A.; Russell, T. P. *Macromolecules* **2010**, *43*, 3844.
- (12) Shin, K.; Woo, E.; Jeong, Y. G.; Kim, C.; Huh, J.; Kim, K. W. *Macromolecules* **2007**, *40*, 6617.
- (13) García-Gutiérrez, M.; Linares, A.; Hernández, J. J.; Rueda, D. R.; Ezquerra, T. A.; Poza, P.; Davies, R. J. *Nano Lett.* **2010**, *10*, 1472.
- (14) Martín, J.; Mijangos, C.; Sanz, A.; Ezquerra, T. A.; Nogales, A. *Macromolecules* **2009**, *42*, 5395.
- (15) Duran, H.; Steinhart, M.; Butt, H.; Floudas, G. *Nano Lett.* **2011**, *11*, 1671.
- (16) Woo, E.; Huh, J.; Jeong, Y. G.; Shin, K. *Phys. Rev. Lett.* **2007**, *98*, 136103.
- (17) Steinhart, M.; Göring, P.; Dernaika, H.; Prabhakaran, M.; Gösele, U. *Phys. Rev. Lett.* **2006**, *97*, 027801.
- (18) Son, J. Y.; Shin, Y.; Song, S.; Shin, Y.; Jang, H. M. *J. Phys. Chem. C* **2011**, *115*, 14077.
- (19) Guan, F.; Yang, L.; Wang, J.; Guan, B.; Han, K.; Wang, Q.; Zhu, L. *Adv. Funct. Mater.* **2011**, *21*, 3176.
- (20) Wang, Y.; Ge, S.; Rafailovich, M.; Sokolov, J.; Zou, Y.; Ade, H.; Lüning, J.; Lustiger, A.; Maron, G. *Macromolecules* **2004**, *37*, 3319.
- (21) Steinhart, M.; Wendorff, J. H.; Greiner, A.; Wehrspohn, R. B.; Nielsch, K.; Schilling, J.; Choi, J.; Gösele, U. *Science* **2002**, *296*, 1997.
- (22) Zhang, M.; Dobriyal, P.; Chen, J. T.; Russell, T. P. *Nano Lett.* **2006**, *6*, 1075.
- (23) Lee, J. I.; Cho, S. H.; Park, S.-M.; Kim, J. K.; Kim, J. K.; Yu, J.-W.; Kim, Y. C.; Russell, T. P. *Nano Lett.* **2008**, *8*, 2315.
- (24) Masuda, H.; Fukuda, K. *Science* **1995**, *268*, 1466.
- (25) Martín, J.; Mijangos, C. *Langmuir* **2009**, *25*, 1181.
- (26) Nielsch, K.; Choi, J.; Schwirn, K.; Wehrspohn, R. B.; Gösele, U. *Nano Lett.* **2008**, *2*, 677.
- (27) Choi, K.; Park, S. H.; Song, Y. M.; Lee, Y. T.; Hwangbo, C. K.; Yang, H.; Lee, H. S. *Adv. Mater.* **2010**, *22*, 3713.
- (28) de Gennes, P. G. *Rev. Mod. Phys.* **1985**, *57*, 827.
- (29) Wang, J.; Li, H.; Liu, J.; Duan, Y.; Jiang, S.; Yan, S. *J. Am. Chem. Soc.* **2003**, *125*, 1496.
- (30) Kang, S. J.; Park, Y. J.; Hwang, J.; Jeong, H. J.; Lee, J. S.; Kim, K. J.; Kim, H.-C.; Huh, J.; Park, C. *Adv. Mater.* **2007**, *19*, 581.
- (31) Benz, M.; Euler, W. B.; Gregory, O. J. *Macromolecules* **2002**, *35*, 2682.
- (32) Petermann, J.; Gohil, R. M. *J. Mater. Sci.* **1979**, *14*, 2260.
- (33) Bune, A. V.; Fridkin, V. M.; Ducharme, S.; Blinov, L. M.; Palto, S. P.; Sorokin, A. V.; Yudin, S. G.; Zlatkin, A. *Nature* **1998**, *391*, 874.
- (34) Naber, R. C. G.; Blom, P. W. M.; Marsman, A. W.; De Leeuw, D. M. *Appl. Phys. Lett.* **2004**, *85*, 2032.
- (35) Zhang, Q. M.; Xu, H.; Fang, F.; Cheng, Z.-Y.; You, H. J. *Appl. Phys.* **2001**, *89*, 2613.
- (36) Xia, F.; Xu, H. H.; Razavi, B.; Cheng, Z.-Y.; Zhang, Q. M. *J. Appl. Phys.* **2002**, *92*, 3111.
- (37) Kang, S. J.; Park, Y. J.; Bae, I.; Kim, K. J.; Kim, H.-C.; Bauer, S.; Thomas, E. L.; Park, C. *Adv. Funct. Mater.* **2009**, *19*, 2812.
- (38) Park, Y. J.; Kang, S. J.; Lotz, B.; Brinkmann, M.; Thierry, A.; Kim, K. J.; Park, C. *Macromolecules* **2008**, *41*, 8648.